Towards high throughput and low-order aberration robustness for vortex coronagraphs with central obstructions

Fogarty, Kevin, Mawet, Dimitri, Mazoyer, Johan, Sirbu, Dan, Ruane, Garreth, et al.

SPIE.

Towards High Throughput and Low-Order Aberration Robustness for Vortex Coronagraphs with Central Obstructions

Kevin Fogarty[a,b], Dimitri Mawet[b], Johan Mazoyer[c,d], Dan Sirbu[a], Garreth Ruane[c], Laurent Pueyo[e]

[a] NASA Ames Research Center, Bldg. 245, Moffett Field, USA
[b] California Institute of Technology, 3500 California Blvd., Pasadena, USA
[c] Jet Propulsion Laboratory, 4800 Oak Grove Dr., Pasadena, USA
[d] Lab. d'Etudes Spatiales et d'Instrumentation en Astrophysique, Observatoire de Paris, Paris, France
[e] Space Telescope Science Institute, 3700 San Martine Dr., Baltimore USA

ABSTRACT

In order to maximize the potential of the next-generation of large space-based observatory to detect and characterize Earth-like exoplanets, coronagraphs must be designed that can obtain high ($\sim 10^{-10}$) contrasts in the presence of realistic low-order aberrations and finite stellar diameters. Unfortunately, for telescopes with central obstructions, maintaining aberration robustness for most coronagraph designs entails significant losses in either throughput or inner working angle. This has resulted in stringent limitations for exo-Earth yields on planned future on-axis telescopes, such as LUVOIR-A. We address this limitation with modified versions of apodized charge 6 and charge 8 vortex coronagraphs which use multiple stages of focal plane mask. These multi-stage apodized vortex coronagraphs (MSAVCs) produce dark holes with contrast $< 10^{-10}$ and mitigate the flux due to tip/tilt offsets as large as 0.05 λ/D while obtaining core throughputs that are a factor of ~ 2 higher than similarly constrained single-stage apodized vortex coronagraphs. The MSAVCs we present are robust to several low-order aberrations, and we discuss the possibility of explicitly constraining low-order aberrations further. Furthermore, we demonstrate mitigating flux due to misalignment between focal plane masks, thus overcoming a significant hurdle in implementing multi-stage vortex designs. By using a parametric expression to estimate the yield of a charge 6 MSAVC for a 10% central obstruction relative to an off-axis charge 6 vortex coronagraph on an 8-m telescope, we estimate it may be possible to retain $\sim 67\%$ of the off-axis yield.

Keywords: coronagraph, vortex coronagraph, direct imaging, low-order aberrations, on-axis telescope, pupil apodization

1. INTRODUCTION

Direct imaging of exoplanets– using adaptive optics in combination with a coronagraph to suppress light from a star in order to reveal its orbiting companions– offers a promising route to discovering and characterizing terrestrial exoplanets.[1–3] This technique has several distinct advantages, including the ability to resolve and separate individual planets in a wide variety of orbital configurations, and to characterize atmospheres in combination with spectroscopy.[4] Proposed future generations of space telescope such as LUVOIR or Habex will enable us to build on these capabilities to characterize the atmospheres of rocky exoplanets and potentially detect biosignatures.[5–7]

Efforts to develop coronagraphs for future space mission concepts need to take into account the impact of complex telescope pupils on contrast and stability. In particular, coronagraphic performance is highly affected by central obstructions, and Stark et al. 2019[8] recently showed that for the terrestrial exoplanet "yield" (i.e. the number of earthlike planets estimated to be detected and characterized over the course of a fixed-duration mission) to reach 30, an off-axis telescope with a coronagraph needs to have an inscribed primary diameter of

---

Further author information, send correspondence to Kevin Fogarty: E-mail: kfogarty@caltech.edu

$\geq$ 7m, but that an on-axis telescope does not achieve this yield until the inscribed diameter is $\geq$ 10m. Closing this yield gap is critical for allowing us to take advantage of the larger primary mirrors made feasible by on-axis designs.

One of the major outstanding problems in coronagraph design is therefore how to recover the lost yield for on-axis telescopes. Existing coronagraphs are either too sensitive to low-order aberrations (LOAs) and stellar angular size to be useful for large-diameter on-axis telescopes, such as the vector vortex coronagraph or the phase-induced amplitude apodization (PIAA) coronagraph, or have a combination of limited throughput, bandwidth, or large inner working angle (IWA), such as the apodized pupil Lyot coronagraph (APLC).[9–17] In order to recover lost on-axis yield, we need to find coronagraph designs that maximize throughput, bandwidth, and IWA while minimizing sensitivity to LOAs and stellar angular size.

In this paper, we propose a modified version of the polynomial apodized vortex coronagraph (PAVC)[13] that partially solves this problem by delivering improved throughput and a small IWA in the presence of central obstructions with radii 10-15% the radius of the pupil while also being robust to LOAs and stellar angular size. The multi-stage apodized vortex coronagraph (MSAVC) uses a pair of opposite-charge vortex focal plane masks (FPMs) in combination with an optimized pupil-plane apodization to create a dark hole with a $< 10^{-10}$ contrast and to limit the residual flux in the image plane due to LOAs and stellar angular size. The MSAVC is based on already-existing apodized vortex coronagraph and multi-stage vortex coronagraph concepts that have been studied extensively.[13, 18–21]

Like other variations of the vortex coronagraph, the MSAVC is inherently broadband and has a relatively aggressive IWA that is determined by the topological charge of the vortex.[22] In this paper we are interested in overcoming the impact of the central obstruction, so we present one-dimensional apodization profiles for the MSAVC. The one-dimensional designs we present are inherently azimuthally symmetric, allowing for full 360° dark holes. In a forthcoming paper we will present full two-dimensional results for MSAVCs explicitly designed for the LUVOIR-A pupil. Mazoyer et al. 2018a,b[23, 24] demonstrate that adaptive optics corrections for struts and spiders in the pupil using a pair of deformable mirrors (DMs) has a sub-dominant effect on LOA sensitivity relative to the coronagraph, so we expect the one-dimensional results presented here to be representative of the performance of the MSAVC on complex pupils with a central obstruction.

The MSAVC represents a trade-off between performance and design complexity, so may be significantly more difficult to implement than previously tested coronagraphs using only a single FPM. However, the MSAVC demonstrates that there are practical solutions to the on-axis lost yield problem that can be found by expanding on well-studied coronagraph technologies. By building on ideas like the MSAVC, we hope to find systems that close the yield gap between on-axis and off-axis designs.

This paper is organized as follows– in Section 2 we describe the optical layout of the MSAVC and the optimization problem for finding combinations of apodization profile and Lyot stop sizes that maximizes transmission through the system while constraining the dark hole and residual flux from LOAs and stellar angular size. We also introduce constraints that limit the residual flux in the image plane produced by misalignment of the optical axes of the two FPMs, which directly addresses the alignment difficulties that affect the multi-stage vortex coronagraph.[25, 26] In Section 3 we present results for MSAVCs using charge 6 FPMs and for MSAVCs using charge 8 FPMs that have been optimized for 10% and 15% central obstructions. We present designs that produce dark holes with $< 10^{-10}$ contrast in the presence of LOAs, as well as designs that have the same sensitivity to on-axis starlight and aberrations to leading order as a vortex coronagraph on a monolithic pupil. In Section 4 we discuss the implications the MSAVC has on the prospects for recovering on-axis telescope yield and highlight future efforts that build on this design exercise, and we summarize our conclusions in Section 5.

2. MSAVC SETUP AND OPTIMIZATION

The layout of the MSAVC is shown in Figure 1. It consists of a pupil plane apodizer (Stage A in Figure 1), which imposes an apodization profile $A(r)$ on the centrally obstructed pupil. The pupil is parameterized by the radius of the central obstruction imposed by the on-axis secondary (R_S) and the pupil radius (R_P). The pupil apodizer is followed in the focal plane in Stage B by the first FPM, which is a vortex phase mask with topological charge c. The vortex mask adds a phase ramp of the form $e^{ic\theta_k}$ to the electric field in stage B (where (r, θ) is

A — Apodized Pupil: $A(r)$ B — Vortex (Charge +6)   C — First Lyot Plane   D — Vortex (Charge -6)   E — Second Lyot Plane
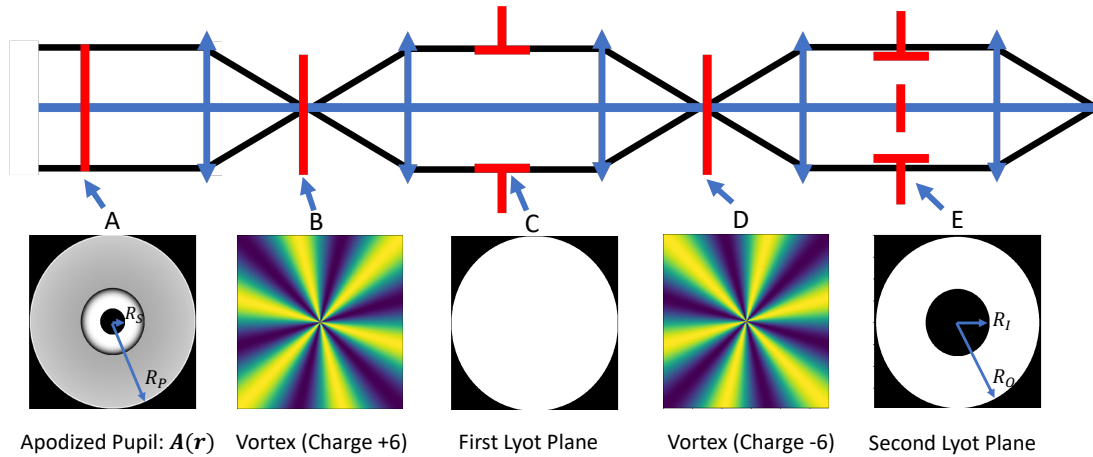
Figure 1. Layout of the MSAVC. At Stage A, light from a centrally obstructed pupil with radius R_P and obstruction radius R_S passes through an apodizer with a transmission function $A(r)$. At Stage B, in the first focal plane, the image of the apodized, obstructed pupil is multiplied by a vortex FPM. In the example shown, the phase ramp has a charge $c = 6$. At Stage C, in the first Lyot plane, a Lyot stop blocks light outside a radius R_P. The second focal plane is at Stage D, where the resulting image is multiplied by a flipped version of the FPM in Stage B, so if $c = 6$ for the FPM in Stage B, $c = -6$ for the FPM in Stage D. Finally, another Lyot stop in the second Lyot plane and Stage E blocks light outside the region $R_I \leq r \leq R_O$, before the beam is focused onto the final image in the detector.

the system of polar coordinates centered on the optical axis in the pupil plane) and (k, θ_k) is the system of polar coordinates centered on the pointing direction in the focal plane). The next stage is the first Lyot plane (Stage C), where a Lyot stop blocks all light outside R_P. This is followed by a second focal plane (Stage D), with an FPM of charge $-c$ (i.e. a phase ramp of the form $e^{-ic\theta_k}$, and a second Lyot plane (Stage E). The Lyot stop in the second Lyot plane allows light to pass through an annulus of inner radius $R_I \geq R_S$ and an outer radius $R_O \leq R_P$. The beam is then focused to form the final image.

We chose to parameterize $A(r)$ as a piecewise polynomial, obeying an expression of the form:

$$A(r) = \begin{cases} \sum_{n=0}^{N} a_n r^n, & R_S \leq r < R_I \\ \sum_{n=0}^{N} b_n r^n, & R_I \leq r < R_O \\ \sum_{n=0}^{N} c_n r^n, & R_O \leq r \leq R_P. \end{cases} \tag{1}$$

We chose this parameterization since apodizations that completely suppress on-axis starlight and leading orders of LOAs are of this form. This set of solutions allows, for example, a charge 6 MSAVC on an obstructed pupil to have approximately the same sensitivity to an aberrated or extended on-axis source as a charge 6 vortex coronagraph on a monolithic pupil. Fogarty et al. 2017b[21] showed that this is also the case for the PAVC if extremely aggressive apodizations are used. For the more general linear program discussed below, we find that this parameterization produces solutions that perform as well as optimizing $A(r)$ pixel-by-pixel and is computationally faster.

For each component in $A(r)$ (e.g. $a_n r^n$), we can write the linear expression corresponding to its contribution to the electric field in the final image plane (suppressing the separable angular component for clarity):
(pupil plane → first focal plane)

$$E(k) = a_n \pi \tilde{\lambda} \int_{R_S}^{R_I} r^n H_0 \left(\pi \tilde{\lambda} k r \right) r \, dr \tag{2}$$
$$\equiv a_n E_{FFP}(k)$$

(first focal plane → first Lyot plane)

$$E\left(r\right) = a_n \pi \tilde{\lambda} \int_0^\infty E_{FFP}\left(k\right) H_c\left(\pi \tilde{\lambda} k r\right) k \, dk$$
$$\equiv a_n E_{FLP}\left(r\right)$$

(3)

(first Lyot plane → second focal plane)

$$E\left(k\right) = a_n \pi \tilde{\lambda} \int_{R_S}^{R_P} E_{FLP}\left(r\right) H_c\left(\pi \tilde{\lambda} k r\right) r \, dr$$
$$\equiv a_n E_{SFP}\left(k\right)$$

(4)

(second focal plane → second Lyot plane)

$$E\left(r\right) = a_n \pi \tilde{\lambda} \int_0^\infty E_{SFP}\left(k\right) H_0\left(\pi \tilde{\lambda} k r\right) k \, dk$$
$$\equiv a_n E_{SLP}\left(r\right)$$

(5)

(second Lyot plane → image plane)

$$E\left(k\right) = a_n \pi \tilde{\lambda} \int_{R_I}^{R_O} E_{SLP}\left(r\right) H_0\left(\pi \tilde{\lambda} k r\right) r \, dr$$
$$\equiv a_n E_{\text{Image},n}\left(k, R_S, R_I\right)$$

(6)

where $\tilde{\lambda}$ is the wavelength normalized to the central wavelength of the observed band and H_x is the Hankel transform of order x. In labelling $E_{\text{Image},n}\left(k, R_S, R_I\right)$, we have chosen to make explicit the fact that the final electric field component depends on the fact that the pupil component $a_n r^n$ is non-zero between R_S and R_I in Equation 2. We note that the angular dependence of the image electric field from the FPMs cancel out, so that the full expression of the image electric field is $= E_{\text{Image},n}\left(k, R_S, R_I\right)$.

2.1 The MSAVC Linear Program

The above expression tells us the electric field in the image plane due to the on-axis starlight passing through each component of $A\left(r\right)$. To obtain constraints on the residual flux from LOAs and stellar angular size, we follow Fogarty et al. 2017b[21] and start by expanding the expression for the electric field in the pupil for a point source that is offset by a tilt from the on-axis position by s in λ/D:

$$E\left(r, \theta\right) = A\left(r\right) e^{i 2\pi \tilde{\lambda} s r \cos\theta}$$
$$= A\left(r\right) \sum_{j=0}^\infty \sum_{l=0}^j C_{jl} s^j r^j e^{i(j-2l)\theta},$$

(7)

where

$$C_{jl} \equiv \left(\frac{i\pi\tilde{\lambda}}{2}\right)^j \frac{1}{j!} \binom{j}{l}.$$

(8)

For a given order j of s, for each value k, Equation 2 becomes (again suppressing the angular component)

$$E\left(k\right) = a_n \pi \tilde{\lambda} C_{jl} s^j \left(\int_{R_S}^{R_I} r^{n+j} H_{j-2l}\left(\pi\tilde{\lambda} k r\right) r \, dr\right)$$
$$\equiv a_n s^j E_{FFP,njl}\left(k\right).$$

(9)

The derivation for the image plane electric field then proceeds identically to the derivation in Equations 3 to 6 above, except that we have replaced $E_{FFP}\left(k\right)$ in Equation 3 with $E_{FFP,jk}\left(k\right)$ and in each equation changed the

order of the Hankel transform from H_x to H_{x+j-2l}. We are therefore left with an expression for the electric field in the image plane $E(k, \theta_k) = a_n E_{\text{Image},njl}(k, R_S, R_I) e^{i(j-2l)\theta_k}$ where $E_{\text{Image},njl}(k, R_S, R_I)$ is defined analogously to $E_{\text{Image},n}(k, R_S, R_I)$ in equation 6.

Putting all this together results in a set of linear constraints that depends on the magnitude of s:

$$-10^{-5.5} \leq \frac{1}{f_{peak}} \sum_{n=0}^{N} \left(a_n E_{\text{Image},n}(k, R_S, R_I) + b_n E_{\text{Image},n}(k, R_I, R_O) + c_n E_{\text{Image},n}(k, R_O, R_P) \right) \leq 10^{-5.5}$$

$$-10^{-5.5} \leq \frac{1}{f_{peak}} s \sum_{n=0}^{N} \left(a_n E_{\text{Image}n,1,-1}(k, R_S, R_I) + b_n E_{\text{Image},n,1,-1}(k, R_I, R_O) \right.$$

$$\left. + c_n E_{\text{Image},n,1,-1}(k, R_O, R_P) \right) \leq 10^{-5.5}$$

$$-10^{-5.5} \leq \frac{1}{f_{peak}} s \sum_{n=0}^{N} \left(a_n E_{\text{Image}n,1,1}(k, R_S, R_I) + b_n E_{\text{Image},n,1,1}(k, R_I, R_O) \right.$$

$$\left. + c_n E_{\text{Image},n,1,1}(k, R_O, R_P) \right) \leq 10^{-5.5}$$

etc.

$$\tag{10}$$

where f_{peak} is the peak flux of the star. We write constraints that nominally get a contrast of 10^{-11}, since this ensures that the constrained components of the aberrated field do not add up to $> 10^{-10}$ intensity and so that the contrast remains $< 10^{-10}$ after renormalizing for the apodized stellar flux. We note that setting constraints of 10^{-10} results in apodizations with only $\sim 10-12\%$ higher throughput. This set of constraints can be increased to include whatever order s^j is required of the problem (up to the order that the vortex FPM suppresses with a monolithic pupil). We can repeat this process for any LOA by swapping out the argument of the exponent in 7 for the desired mode to come up with constraints.

We also want to account for the misalignments between the first and second FPMs. Misaligning the two FPMS is equivalent to introducing an additional position offset at the first Lyot plane (Stage C in Figure 1). Starting with the expression for the electric field in the first Lyot plane ($E_{FLP,njl}(r)$, defined analogously to $E_{FFP,njl}(k)$ in Equation 9), the first Lyot plane electric field becomes:

$$E(r, \theta) = E_{FLP,njl}(r) e^{i2\pi\tilde{\lambda}s_{MA}r\cos\theta}$$
$$= E_{FLP,njl}(r) \sum_{m=0}^{\infty} \sum_{p=0}^{m} C_{mp} s_{MA}^m r^m e^{i(m-2p)\theta}, \tag{11}$$

where s_{MA} is the magnitude of the misalignment-induced offset.

The image field due to each component in the expansion of the misalignment-induced tip/tilt in the first Lyot plane on any given aberrated pupil term (including $j, l = 0, 0$ for the unaberrated component) is given by (again, for component $a_n r^n$ of the apodization):

first Lyot plane $\rightarrow$ second focal plane

$$E(k) = a_n \pi \tilde{\lambda} C_{mp} s^j s_{MA}^m \left(\int_{R_S}^{R_P} E_{FLP,njl}(r) r^m H_{c+j-2l+m-2p}\left(\pi\tilde{\lambda}kr\right) r dr \right)$$
$$\equiv a_n s^j s_{MA}^m E_{SFP,njlmp}(k) \tag{12}$$

second focal plane $\rightarrow$ second Lyot plane

$$E(r) = a_n \pi \tilde{\lambda} s^j s_{MA}^m \left(\int_0^\infty E_{SFP,njlmp}(k) H_{j+m-2(l+p)}\left(\pi\tilde{\lambda}kr\right) k dk \right)$$
$$\equiv a_n s^j s_{MA}^m E_{SLP,njlmp}(r) \tag{13}$$

second Lyot plane → image plane

$$E\left(k\right) = a_n \pi \tilde{\lambda} s^j s_{MA}^m \left(\int_{R_I}^{R_O} E_{SLP,njlmp}\left(r\right) H_{j+m-2(l+p)}\left(\pi\tilde{\lambda}kr\right) r dr\right)$$

$$\equiv a_n s^j s_{MA}^m E_{\text{Image},njlmp}\left(k, R_S, R_I\right),$$

(14)

where as before we suppress the angular component. The aberrated image components in Equation 14 results in a set of linear constraints analogous to Equations 10:

$$10^{-5.5} \le \frac{1}{f_{peak}} s_{MA} \sum_{n=0}^{N} \bigg(a_n E_{\text{Image},n,0,0,1,1}\left(k, R_S, R_I\right) + b_n E_{\text{Image},n,0,0,1,1}\left(k, R_I, R_O\right)$$

$$+ c_n E_{\text{Image},n,0,0,1,1}\left(k, R_O, R_P\right)\bigg) \le 10^{5.5}$$

$$10^{-5.5} \le \frac{1}{f_{peak}} s_{MA} \sum_{n=0}^{N} \bigg(a_n E_{\text{Image},n,0,0,1,-1}\left(k, R_S, R_I\right) + b_n E_{\text{Image},n,0,0,1,-1}\left(k, R_I, R_O\right)$$

$$+ c_n E_{\text{Image},n,0,0,1,-1}\left(k, R_O, R_P\right)\bigg) \le 10^{5.5}$$

(15)

etc.

for combinations of j, l, m, p up to the order in $s^j s_{MA}^m$ that needs to be constrained.

The linear program for an MSAVC becomes:

Maximize:

$$T\left(r\right) = \sum_{n=0}^{N} \frac{1}{n+1} b_n \left(R_O^{n+1} - R_I^{n+1}\right)$$

such that:

(16)

$$0 \le A\left(r\right) \le 1,$$

Equations 10 hold true for: Inner Angle $\le k \le$ Outer Angle

Equations 15 hold true for: Inner Angle $\le k \le$ Outer Angle

For the charge 6 MSAVC results we present in this paper, we include constraints for terms below s^3 and s_{MA}^3 in the expansions for Equations 7 and 11, and for charge 8 MSAVC results, we include constraints for terms below s^4 and s_{MA}^4. Fluxes are constrained in a dark hole with an inner angle of 2.5 λ/D and and outer angle of 16 λ/D and we assume a bandwidth of 0.2, although our results do not depend strongly on either the outer angle or the bandwidth.

In order to arrive at the optimal combination of Lyot stop radii (R_I and R_O) and apodizer for each combination of vortex charge and central obstruction size, we performed a Bayesian optimization treating R_I and R_O as hyper-parameters using the python module `hyperopt`. At each iteration of the optimization loop, we ran the linear program described in Equation 16. Then, we calculated the absolute core throughput of a point source at an offset of 3 λ/D^*, and used this quantity as the figure-of-merit to be maximized with `hyperopt`. Since there are only two hyper-parameters for any given combination of vortex charge and central obstruction size, this process settles on optimal values of R_I and R_O within a few hundred iterations.

Because the linear program explicitly sets constraints on the amount of residual flux due to each term in Equations 7 and 11 separately, it limits the residual flux from any offsets $\le s$ and $\le s_{MA}$. Tip/tilt aberrations

---

*throughput in this paper is defined using 'core throughput': the ratio of total intensity of a source in an 0.7 λ/D photometric aperture to the total energy collected by the telescope.

and misalignments shift the position of the on-axis source, so by setting s and s_{MA} to the value of the largest shift we want to be robust to, we successfully constrain the effects of tip/tilt jitter and arbitrary misalignments. Similarly, the light from a star with non-zero angular size can be thought of as being spread out between a collection of incoherent point sources. An MSAVC that meets the constraints this linear problem for an offset s will suppress the light from a star with a radius slightly larger than s.

In this paper, therefore, we are explicitly setting constraints for tip/tilt. However, the same procedure we outline for tip/tilt constraints applies to higher-order LOAs as well. In our subsequent paper we will report on the impact explicitly constraining higher-order LOAs has on MSAVC throughput, and in the current paper we report on the LOA sensitivity of the tip/tilt optimized MSAVC. We also reserve a discussion of focal plane-Lyot plane misalignments for a more in-depth treatment in a later paper.

3. RESULTS

]

We ran optimizations for a charge 6 and 8 MSAVC for both 10% an 15% central obstructions. We constrained the system to limit leaked flux for source offsets of $s \le 0.05\ \lambda/D$ and misalignment offsets of $s_{MA} \le 0.05\ \lambda/D$. We chose this value of s because it will result in an MSAVC that is robust to stellar angular diameters of $\gtrsim 0.1$ λ/D, which is the approximate largest stellar angular diameter that will be observed by LUVOIR-A.[7] We chose this value s_{MA} in order to demonstrate the ability to constrain misalignment sensitivity at least as much as tip/tilt sensitivity.

Apodizations for each version of the MSAVC are shown in Figure 2, and the profiles of the dark holes along with the azimuthally-average residual flux due to tip/tilt and misalignment offsets are shown in Figure 3. For comparison, apodizations and dark holes for charge 6 and 8 PAVCs optimized for the same requirements are shown in Figures 2 and 3 as well. We also show the two-dimensional residual tip/tilt and misalignment fluxes for each version of the MSAVC in Figure 4.

The core throughput of a planet orbiting the on-axis star as a function of its angular separation is shown in Figure 5 for each coronagraph design. We find a throughput of 29.9% for a charge 6 MSAVC optimized for a 10% central obstruction, and 14.9% for a 15% central obstruction. For a charge 8 MSAVC, meanwhile, throughputs are 32.8% and 21.2%, respectively. By comparison, a robust charge 6 PAVC has a throughput of 16.5% for a 10% central obstruction and 7.0% for a 15% central obstruction, while a charge 8 PAVC has throughputs of 18.0% and 12.1%. The throughput of the MSAVC improves over the PAVC by a factor of $\sim 1.8 - 2.1$ for the range of cases studied here.

As is the case with the multi-stage vortex, the additional FPM stage does not strongly affect the IWA of the MSAVC. The charge 6 MSAVC IWA is $\sim 3.25\ \lambda/D$ for the 10% and $\sim 3.5\ \lambda/D$ for the 15% central obstruction, which is $\sim 0.5\ \lambda/D$ better than the corresponding IWA for the PAVC. Increases in the IWA over the unobstructed vortex are driven by increased apodization and inner Lyot stop size, which is why the IWA of the MSAVC is smaller than the robust PAVC. For the charge 8 MSAVC, the IWA is $\sim 4.25 - 4.5\ \lambda/D$.

We note that for the MSAVC, and for coronagraphs incorporating vortex FPMs in general, the IWA as normally defined (i.e. the angular separation where throughput reaches 50% of its maximum value) may be misleading owing to the relatively gradual slope of the throughput curve. The dark hole for the MSAVC designs in this paper provide deep contrasts for separations smaller than the IWA, so planets could be detected at angular separations considerably smaller than the IWA. We could for example consider the smallest angular separation where throughput for a planet is $\ge 5\%$ as a reasonable approximation for the minimum distance where an exoplanet could be observed. With a 10% central obstruction, this distance is 1.5 λ/D for a charge 6 MSAVC and 2.0 λ/D for a charge 8 MSAVC. However, these separations are within 2.5 λ/D, so for a terrestrial exoplanet the minimum distance is $\sim 2.5\ \lambda/D$. Meanwhile, with a 15%, the distance is $\sim 2.25\ \lambda/D$ for both charge 6 and 8. Unlike, for example, an APLC where the IWA is a reasonable approximation for the smallest angular separation where a planet could be observed, the designs we present here could potentially be used to observed planets several λ/D closer to their host stars than the IWA.

We calculated the residual fluxes for several LOAs that vortex coronagraphs with charges ≥ 6 are insensitive to on monolithic pupils, namely tip/tilt, astigmatism, and defocus.[27] Figure 6 shows the mean flux in an annular
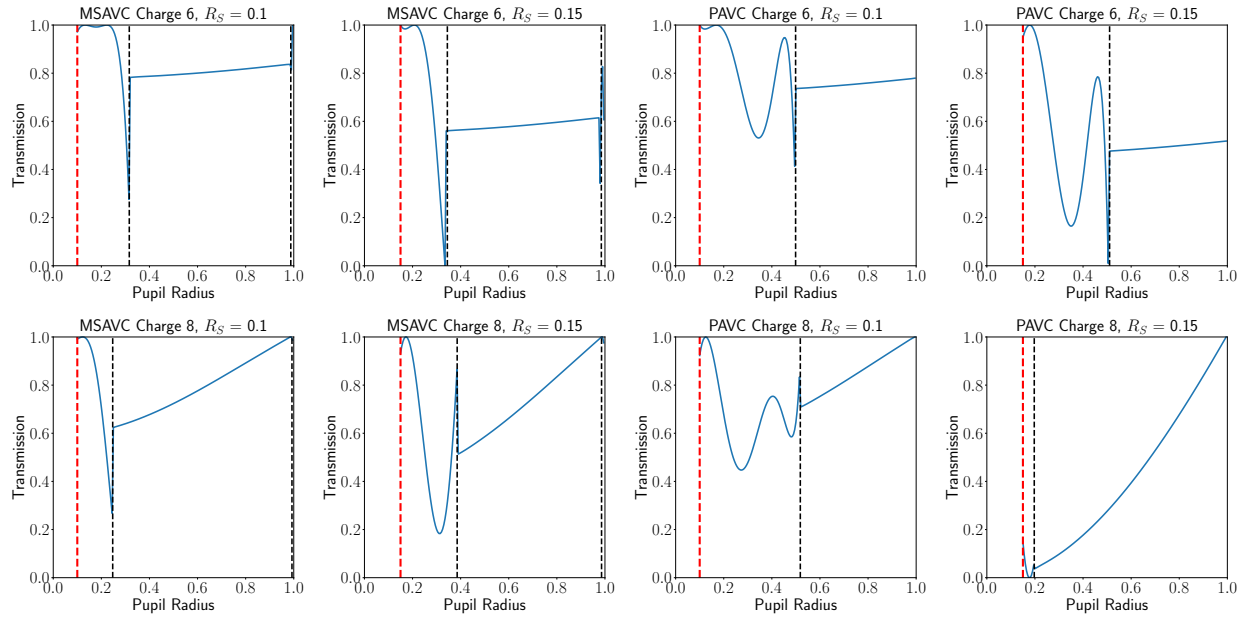
Figure 2. Apodizers for a charge 6 LOA-robust MSAVC and PAVC are shown in the top row, with the left two plots showing $A(r)$ for MSAVCs optimized for 10% and 15% central obstructions, and the right two plots showing $A(r)$ for PAVCs. Apodizers for charge 8 MSAVCs and PAVCs are shown in the bottom row. In each plot, the blue curve represents the function $A(r)$. The red dashed line denotes R_S, while the two black dashed lines in the MSAVC plots denote R_I (the inner Lyot stop radius) and R_O (the outer Lyot stop radius) in the SLP. The black dashed line in the PAVC plots denotes the inner Lyot stop radius in the Lyot plane. Radii are normalized to $R_P = 1$.
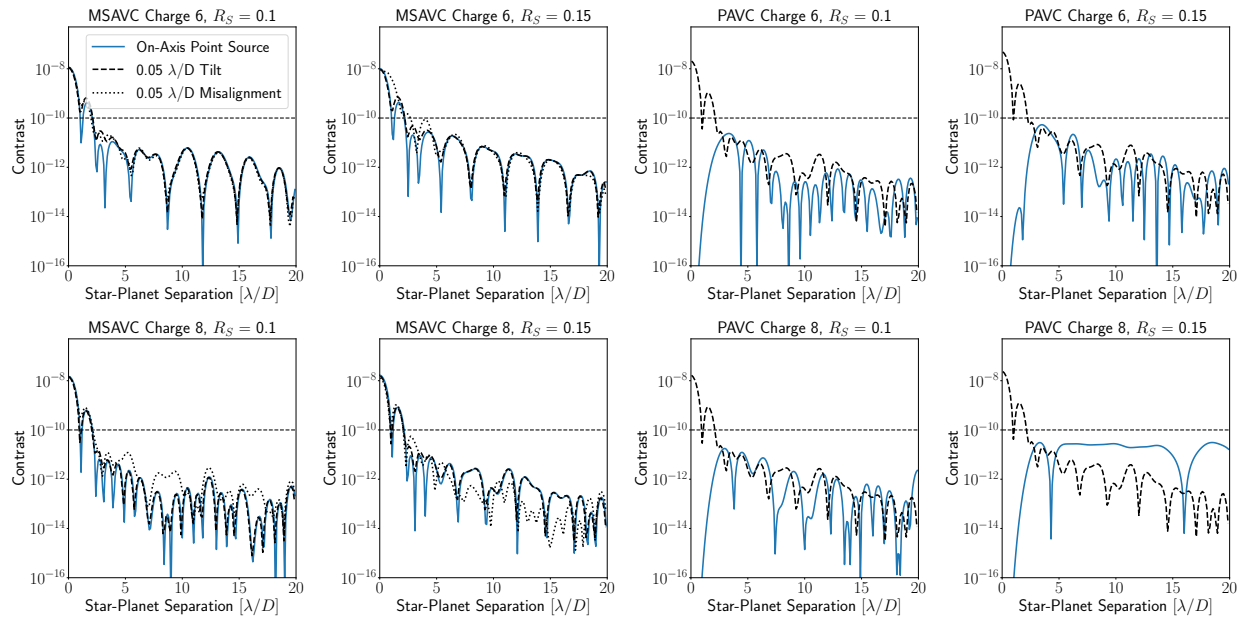

Figure 3. Dark holes corresponding to the MSAVC and PAVC configurations in Figure 2. The blue curves show contrast normalized to the peak PSF flux with the vortex masks out. Black dashed lines show contrast in the presence of an 0.05 λ/D tilt, and black dotted lines show contrast in the presence of an 0.05 λ/D misalignment between the FPMs. FPM misalignment does not apply to the single-stage PAVC.
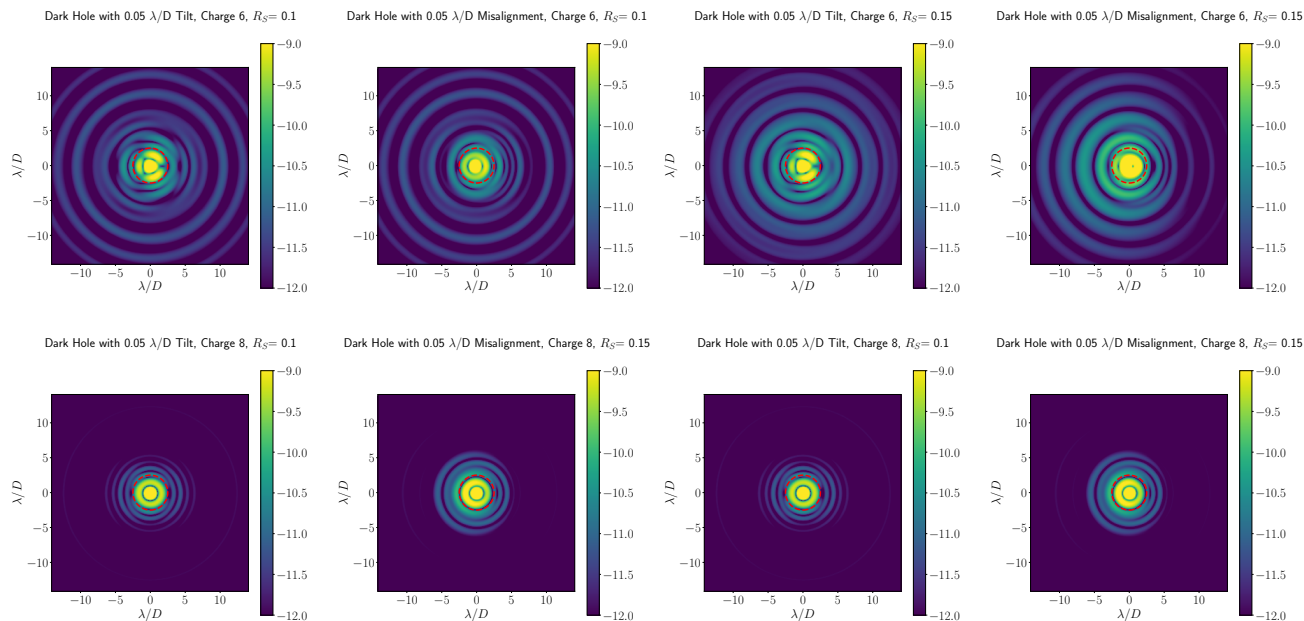
Figure 4. Residual flux in the image plane due to tilts and misalignments for the MSAVCs presented in Figure 2. The top row shows the two-dimensional dark hole with an 0.05 λ/D tilt or FPM misalignment applied to the charge 6 MSAVC, while the bottom row shows the same result for the charge 8 MSAVC. The red circle denotes 2.5 λ/D.
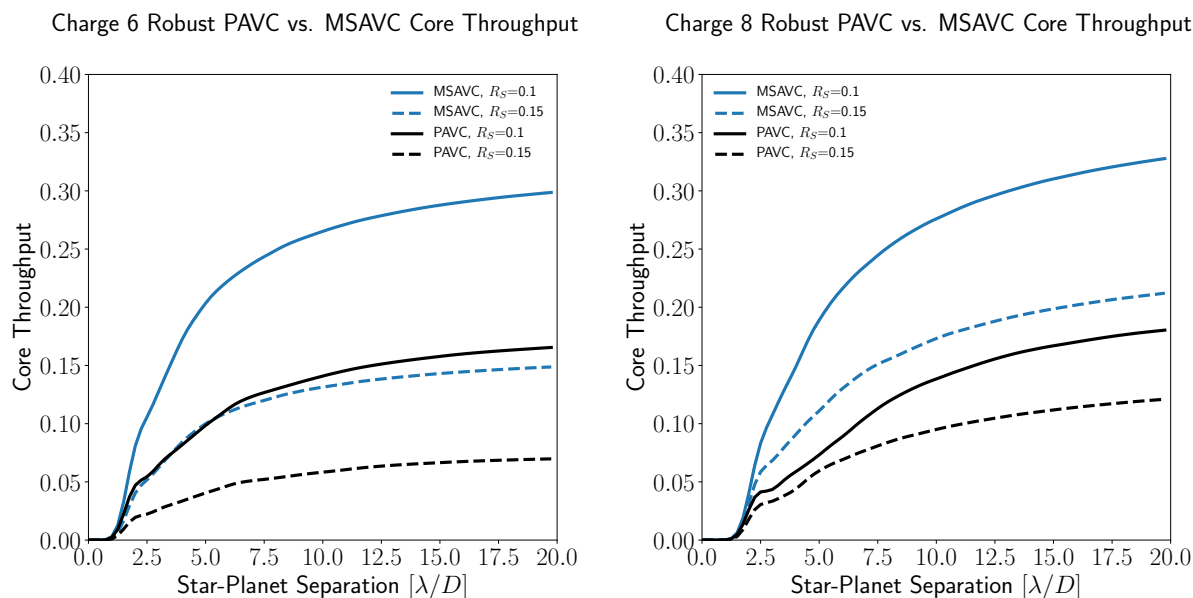

Figure 5. Core throughput for the MSAVC designs displayed in Figure 2, compared to PAVC designs optimized for the same level of tip/tilt robustness. The comparison between charge 6 coronagraphs is shown on the left, and between charge 8 coronagraphs is shown on the right. Blue lines correspond to the MSAVC, black lines to the PAVC, and solid lines show throughput curves for coronagraphs optimized for a 10% central obstruction and dashed lines for coronagraphs optimized for a 15% central obstruction.
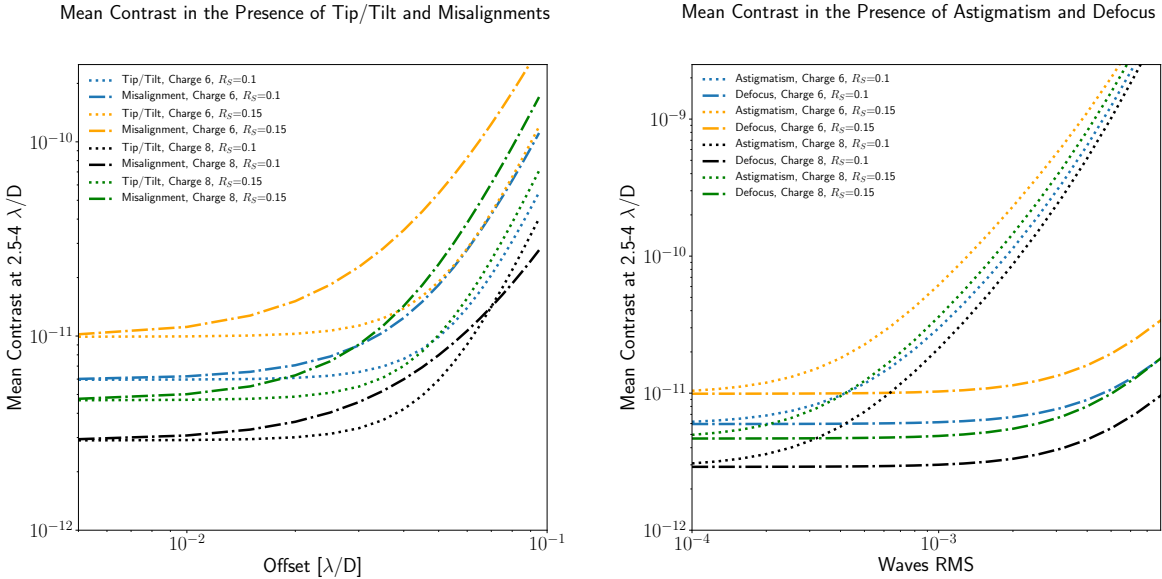
Figure 6. *Left:* Mean contrast in an annular region of 2.5-4 λ/D around the on-axis star as a function of tilt or misalignment offset in λ/D, for charge 6 and 8 MSAVCs with 10% and 15% central obstructions. Sensitivity is not strongly affected by R_S owing to the aberrated pupil flux being explicitly constrained by the optimization problem. *Right:* Same result for defocus and astigmatism aberrated pupils as a function of waves RMS.

region $2.5 - 4 \lambda$/D around the host star for a pupil with an LOA as a function of size of the LOA. The MSAVC is more sensitive to LOAs than a vortex coronagraph on a monolithic pupil; however, it still results in a $< 10^{-10}$ dark hole for aberrations within an order of magnitude of what the charge 6 vortex is sensitive to. Therefore, even when optimized only for tip/tilt, the MSAVC significantly reduces the LOA stability requirements for an on-axis coronagraph. In our forthcoming paper we will discuss the trade-off between MSAVC throughput and LOA performance in detail.

By designing MSAVCs for both 10% and 15% central obstructions, we find that the performance of the coronagraph, both in an absolute sense and relative to a single-stage apodized vortex coronagraph, depends critically on the size of the central obstruction. With the same design constraints, increasing the size of the central obstruction by 50% decreases MSAVC throughput by about a factor of 1.5-2, while IWA and LOA performance are not strongly affected. However, the gain in throughput from using a dual stage instead of a single stage vortex stays relatively unchanged as the radius of the central obstruction increases. This behavior is consistent with the central obstruction being the driving factor behind the sensitivity of the vortex to LOAs and also with the second vortex FPM directly addressing the impact of having a central obstruction.

3.1 Reproducing Vortex Coronagraph Robustness

As we discussed in Section 2, the linear program for the MSAVC can be solved exactly, so as to reproduce the leading-order response of the vortex coronagraph to offsets. With these solutions, for obstructed pupils we can reproduce the starlight suppression and LOA insensitivity of the vector vortex on monolithic pupils.

The analytical derivation of these solutions is similar to the derivation for exact solutions in Fogarty et al. 2017b,[21] but with the additional propagations for the extra stages in the MSAVC. However, not all the terms in the expansion if pupil misalignments have a closed form, so the solutions we present in this section do not account for FPM misalignment.

The core throughput of analytical solutions to the charge 6 MSAVC vs. size of the central obstruction in shown in Figure 7 compared with analytical PAVC solutions. The sensitivity of the charge 6 coronagraphs shown here to low-order aberrations goes as s^6 to leading order where s is the amplitude of the aberration, which is the

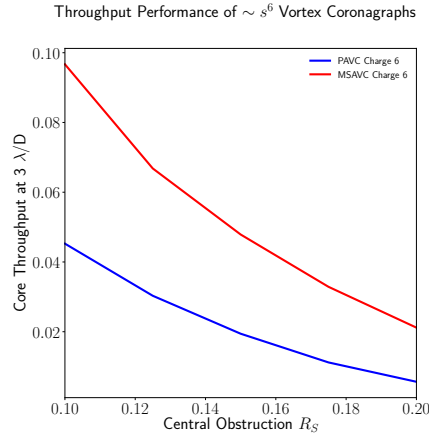Throughput Performance of $\sim s^6$ Vortex Coronagraphs

Figure 7. Core throughput at 3 λ/D of charge 6 MSAVCs that have the same aberrations sensitivity of the VC on a monolithic pupil, to leading order. Similarly optimized PAVCs are shown for comparison. The blue line shows the performance of the PAVC as a function of R_S, and the red line show the performance of the MSAVC.

same leading-order behavior as an unobstructed vortex.[28] In principle, there exist a family of charge 8 single- and multi-stage coronagraphs that go as s^8 to leading order, but these offer very low transmission through the apodizer. Even for charge 6, the low throughput limits the practical applications of these exact solutions. Throughput diminishes as a function of central obstruction radius, but decreases more rapidly for smaller central obstructions than larger ones. This suggests that making a relatively small ($\sim 10\%$) central obstruction slightly smaller may lead to significant gains in throughput, whereas making a larger central obstruction slightly smaller may not change coronagraphic performance by as much.

4. DISCUSSION

4.1 Impact of the MSAVC on Yield

The purpose of the coronagraph design discussed in this paper is to address the under-performance of coronagraphs on on-axis telescopes compared to off-axis telescopes. The on-axis and off-axis coronagraph concepts studied in Stark et al. 2019[8] showed that the yield for an on-axis telescope underperforms relative to an off-axis telescope of the same pupil diameter by a factor of ~ 2. The MSAVC is an approach to relaxing tension between throughput, IWA, bandwidth, and aberration sensitivity that drive this under-performance.

In order to approximate the impact of the MSAVC on yield, we can use the power-law indices derived in Stark et al. 2019[8] that approximate the dependence of yield on various parameters of the coronagraph to extrapolate from the yield of an off-axis charge 6 vortex coronagraph, which is based on the DM-assisted off-axis vortex coronagraph discussed in Ruane et al. 2018.[29] The comparison between the two systems is apt because the setups are similar– the differences between the two are the greyscale pupil apodization and the additional vortex and Lyot stage are different. The bandwidth is identical, and the shape of the throughput curve (and therefore how changing the IWA translates to changes in yield) are similar for both sorts of system. Moreover, as stated above, Mazoyer et al. 2018a, b[23, 24] demonstrates that suppressing pupil segment gaps and spiders by using pairs of DMs has a second-order effect on LOA sensitivity compared to the sensitivity of the coronagraph itself. Therefore, the strategy of using a pair of DMs to suppress gaps and spiders in a segmented off-axis pupil provides a rough approximation for how a full 2-D treatment of the MSAVC will impact yield.

We estimate that the yield of the charge 6 MSAVC optimized for a 10% central obstruction on an 8-m diameter telescope (i.e. the pupil diameter of the off-axis case studied in Stark et al. 2019[8]) is approximately

$$\frac{\text{Yield}_{\text{MSAVC}}}{\text{Yield}_{\text{Off-Axis}}} = \left(\frac{T_{\text{MSAVC}}}{T_{\text{Off-Axis}}}\right)^{0.39} \left(\frac{IWA_{\text{MSAVC}}}{IWA_{\text{Off-Axis}}}\right)^{-0.38} = 0.67, \tag{17}$$

where T is throughput. For $T_{\text{Off-Axis}}$ we do not account for the effects of DM corrections since we assume the MSAVC would incur similar losses from DM corrections and therefore use the core throughput of a charge 6 vortex coronagraph. For a 15% central obstruction, the charge 6 MSAVC would provide ~ 0.525 of the yield of the vortex coronagraph on an off-axis pupil. Therefore, at least for a 10% central obstruction, the charge 6 MSAVC significantly reduces the factor of ~ 2 yield degradation an 8-m on-axis telescope experiences relative to an off-axis telescope.

It is important to emphasize that this is a rough approximation based on extrapolating from yields estimated for a different system, and that the power law indices derived in Stark et al. 2019[8] are only valid in the immediate vicinity in parameter space to the points where they were estimated. For our approximation for a charge 6 MSAVC the throughput curve is similar to a charge 6 vortex coronagraph, and we only argue that our estimate is plausible for an 8-m telescope in order to use the indices adopted in Equation 17. It is not safe to assume, for example, that based on our analysis the charge 6 MSAVC achieves 67% of the yield of an off-axis charge 6 vortex for a 15-m diameter primary. Bearing this caveat in mind, we conclude that for an 8-m diameter telescope, the MSAVC can potentially "fill in" part of the gap between current on-axis and off-axis coronagraph designs. If the MSAVC achieves similar gains in yield for larger primary diameters, it would significantly increase the number of terrestrial exoplanets observed by proposed on-axis telescopes such as LUVOIR-A with larger primary mirrors.

4.2 Implementation of the MSAVC

The MSAVC is primarily meant as a design exercise to push the limits of coronagraph capability on on-axis telescopes. However, we have demonstrated that the difficulty previous dual-stage vortex coronagraph implementations had with aligning cascading FPMs can be mitigated by writing constraints on residual flux due to FPM misalignments. One of the advantages of explicitly optimizing for LOA and misalignment sensitivity is that it opens a trade space between coronagraph throughput and contrast and telescope stability requirements that can be directly explored. This suggests that the added complexity of having multiple focal plane stages can potentially be addressed, if the drawbacks of that added complexity can be outweighed by the advantages of a multi-stage coronagraph in terms of yield.

A further application of this result could potentially be for ground-based coronagraphy where FPM alignment is more feasible. The apodization problem we solve for a space-based coronagraph delivering a $< 10^{-10}$ contrast dark hole can be applied to ground-based telescopes that incorporate multiple vortex stages. Using the formalism in this paper, it is straightforward to compute apodization profiles that meet design requirements set by how precisely the FPMs need to be aligned.

5. CONCLUSION

We presented one-dimensional apodization profiles for the MSAVC. The MSAVC is a coronagraph that builds on previous work with apodized vortex coronagraphs[13, 20, 21] and dual-stage vortex coronagraphs[18, 19] with the goal of simultaneously maximizing throughput, contrast, and LOA robustness in the presence of a central obstruction while maintaining the broadband and small IWA characteristics of the vortex coronagraph. The purpose of this effort is to find examples of coronagraph designs that address the terrestrial exoplanet yield inefficiency of proposed on-axis telescopes. We outlined a linear program that can be used to compute apodization profiles that maximize transmission while obtaining $< 10^{-10}$ contrast in a dark hole and constraining the residual flux from stellar angular size and LOAs to below a target threshold. We also implemented constraints that limited the residual flux due to misalignments between the FPMs.

We solved the optimization problem for charge 6 and 8 vortex masks, and for 10% and 15% central obstructions. In each case, the MSAVC was optimized to suppress the residual flux from point source and misalignment offsets as large as 0.05 λ/D to below 10^{-11} relative to the on-axis star. Compared to PAVCs optimized with similar constraints, the MSAVC obtains a factor of $1.8 - 2.1$ higher throughput, and a slightly smaller IWA. The designs we present are also relatively insensitive to other LOAs, which we demonstrate by computing the dark hole flux in the presence of astigmatism and defocus. We also demonstrated that, on a centrally obstructed pupil, the charge 6 MSAVC can reproduce the sensitivity of the charge 6 vortex coronagraph on a monolithic pupil using an analytic formulation of the optimization problem. However, these solutions require aggressive apodization and do not explicitly constrain sensitivity to FPM misalignment.

The MSAVC demonstrates an example of a coronagraph with the potential to increase the yield of on-axis telescopes over current coronagraph designs. We extrapolated from the off-axis vortex coronagraph designed for an 8-m telescope studied in[8] using the parameterization of yield as a function of coronagraph characteristics studied in that paper. As a rough approximation, we estimate that a charge 6 MSAVC would retain approximately 67% of the yield of the off-axis vortex for a 10% central obstruction, which suggests that the MSAVC could get about half of the way towards closing the gap between the off-axis and on-axis design. While the MSAVC represents a significant improvement in throughput and aberration sensitivity over previous apodized vortex coronagraphs, performance still depends critically on the size of the central obstruction. Therefore, the MSAVC does not entirely solve the problem of the trade-off between throughput and aberration sensitivity.

This paper presents the proof-of-concept for the MSAVC. A full treatment of two dimensional pupils, more precise yield estimates, and explicit optimization of sensitivity to higher-order LOAs, such as astigmatism and defocus, will be discussed in a forthcoming paper. The MSAVC is a useful starting point for exploring modifications to existing coronagraph designs that will achieve significant improvements in on-axis telescope yield. Currently, we are exploring several avenues, such as the using PIAA-style shaped mirrors in combination with the vortex coronagraph, in order to push the boundaries of terrestrial exoplanet yields and maximize our potential to detect biosignatures with future space telescopes.

REFERENCES

[1] Stark, C. C., Roberge, A., Mandell, A., Clampin, M., Domagal-Goldman, S. D., McElwain, M. W., and Stapelfeldt, K. R., "Lower Limits on Aperture Size for an ExoEarth Detecting Coronagraphic Mission," *ApJ* **808**, 149 (Aug. 2015).

[2] Dalcanton, J., Seager, S., Aigrain, S., Battel, S., Brandt, N., Conroy, C., Feinberg, L., Gezari, S., Guyon, O., Harris, W., Hirata, C., Mather, J., Postman, M., Redding, D., Schiminovich, D., Stahl, H. P., and Tumlinson, J., "From Cosmic Birth to Living Earths: The Future of UVOIR Space Astronomy," *arXiv e-prints* , arXiv:1507.04779 (July 2015).

[3] Shaklan, S., Crill, B., Belikov, R., Bryson, S., Bendek, E., Bolcar, M., Fogarty, K., Krist, J., Mawet, D., Mejia Prada, C., Mazoyer, J., N'Diaye, M., Noss, J., Juanola-Parramon, R., Por, E., Riggs, A. J. E., Ruane, G., Siegler, N., Sirbu, D., Sivaramakrishnan, A., Soummer, R., St. Laurent, K., Stark, C., and Zimmerman, N., "Status of Space-based Segmented-Aperture Coronagraphs for Characterizing Exo-Earths Around Sun-Like Stars," in [*Bulletin of the American Astronomical Society*], **51**, 211 (Sept. 2019).

[4] Stark, C. C., Dressing, C., Dulz, S., Lopez, E., Marley, M. S., Plavchan, P., and Sahlmann, J., "Toward Complete Characterization: Prospects for Directly Imaging Transiting Exoplanets," *AJ* **159**, 286 (June 2020).

[5] Bolcar, M. R., Balasubramanian, K., Clampin, M., Crooke, J., Feinberg, L., Postman, M., Quijada, M., Rauscher, B., Redding, D., Rioux, N., Shaklan, S., Stahl, H. P., Stahle, C., and Thronson, H., "Technology development for the Advanced Technology Large Aperture Space Telescope (ATLAST) as a candidate large UV-Optical-Infrared (LUVOIR) surveyor," in [*Optics for EUV, X-Ray, and Gamma-Ray Astronomy VII*], MacEwen, H. A. and Breckinridge, J. B., eds., *Society of Photo-Optical Instrumentation Engineers (SPIE) Conference Series* **9602**, 960209 (Sept. 2015).

[6] Wang, J., Mawet, D., Hu, R., Ruane, G., Delorme, J.-R., and Klimovic, N., "Baseline Requirements For Detecting Biosignatures with the HabEx and LUVOIR Mission Concepts," *ArXiv e-prints* (June 2018).

[7] The LUVOIR Team, "The LUVOIR Mission Concept Study Final Report," *arXiv e-prints* , arXiv:1912.06219 (Dec. 2019).

[8] Stark, C. C., Belikov, R., Bolcar, M. R., Cady, E., Crill, B. P., Ertel, S., Groff, T., Hildebrandt, S., Krist, J., Lisman, P. D., Mazoyer, J., Mennesson, B., Nemati, B., Pueyo, L., Rauscher, B. J., Riggs, A. J., Ruane, G., Shaklan, S. B., Sirbu, D., Soummer, R., Laurent, K. S., and Zimmerman, N., "ExoEarth yield landscape for future direct imaging space telescopes," *Journal of Astronomical Telescopes, Instruments, and Systems* **5**, 024009 (Apr 2019).

[9] Soummer, R., "Apodized Pupil Lyot Coronagraphs for Arbitrary Telescope Apertures," *ApJL* **618**, L161–L164 (Jan. 2005).

[10] N'Diaye, M., Pueyo, L., and Soummer, R., "Apodized Pupil Lyot Coronagraphs for Arbitrary Apertures. IV. Reduced Inner Working Angle and Increased Robustness to Low-order Aberrations," *ApJ* **799**, 225 (Feb. 2015).

[11] Fogarty, K., Mazoyer, J., St. Laurent, K., Soummer, R., N'Diaye, M., Stark, C., and Pueyo, L., "Optimal deformable mirror and pupil apodization combinations for apodized pupil Lyot coronagraphs with obstructed pupils," in [*proc. SPIE*], *Society of Photo-Optical Instrumentation Engineers (SPIE) Conference Series* **10698**, 106981J (Aug 2018).

[12] Ruane, G., Jewell, J., Mawet, D., Pueyo, L., and Shaklan, S., "Apodized vortex coronagraph designs for segmented aperture telescopes," in [*Advances in Optical and Mechanical Technologies for Telescopes and Instrumentation II*], *proc. SPIE* **9912**, 99122L (July 2016).

[13] Fogarty, K., Pueyo, L., Mazoyer, J., and N'Diaye, M., "Polynomial Apodizers for Centrally Obscured Vortex Coronagraphs," *AJ* **154**, 240 (Dec 2017).

[14] Guyon, O., "Phase-induced amplitude apodization of telescope pupils for extrasolar terrestrial planet imaging," *A&A* **404**, 379–387 (June 2003).

[15] Traub, W. A. and Vanderbei, R. J., "Two-Mirror Apodization for High-Contrast Imaging," *ApJ* **599**, 695–701 (Dec. 2003).

[16] Guyon, O., Pluzhnik, E. A., Galicher, R., Martinache, F., Ridgway, S. T., and Woodruff, R. A., "Exoplanet Imaging with a Phase-induced Amplitude Apodization Coronagraph. I. Principle," *ApJ* **622**, 744–758 (Mar. 2005).

[17] Guyon, O., Hinz, P. M., Cady, E., Belikov, R., and Martinache, F., "High Performance Lyot and PIAA Coronagraphy for Arbitrarily Shaped Telescope Apertures," *ApJ* **780**, 171 (Jan. 2014).

[18] Serabyn, E., Mawet, D., Wallace, J. K., Liewer, K., Trauger, J., Moody, D., and Kern, B., [*Recent progress in vector vortex coronagraphy*], vol. 8146 of *Society of Photo-Optical Instrumentation Engineers (SPIE) Conference Series*, 81460L (2011).

[19] Mawet, D., Serabyn, E., Wallace, J. K., and Pueyo, L., "Improved high-contrast imaging with on-axis telescopes using a multistage vortex coronagraph," *Optics Letters* **36**, 1506 (Apr 2011).

[20] Mawet, D., Pueyo, L., Carlotti, A., Mennesson, B., Serabyn, E., and Wallace, J. K., "Ring-apodized Vortex Coronagraphs for Obscured Telescopes. I. Transmissive Ring Apodizers," *ApJS* **209**, 7 (Nov. 2013).

[21] Fogarty, K., Pueyo, L., Mazoyer, J., and N'Diaye, M., "Tip/tilt optimizations for polynomial apodized vortex coronagraphs on obscured telescope pupils," in [*proc. SPIE*], *Society of Photo-Optical Instrumentation Engineers (SPIE) Conference Series* **10400**, 104000T (Sep 2017).

[22] Mawet, D., Riaud, P., Absil, O., and Surdej, J., "Annular Groove Phase Mask Coronagraph," *ApJ* **633**, 1191–1200 (Nov. 2005).

[23] Mazoyer, J., Pueyo, L., N'Diaye, M., Fogarty, K., Zimmerman, N., Leboulleux, L., St. Laurent, K. E., Soummer, R., Shaklan, S., and Norman, C., "Active Correction of Aperture Discontinuities-Optimized Stroke Minimization. I. A New Adaptive Interaction Matrix Algorithm," *AJ* **155**, 7 (Jan. 2018).

[24] Mazoyer, J., Pueyo, L., N'Diaye, M., Fogarty, K., Zimmerman, N., Soummer, R., Shaklan, S., and Norman, C., "Active Correction of Aperture Discontinuities-Optimized Stroke Minimization. II. Optimization for Future Missions," *AJ* **155**, 8 (Jan. 2018).

[25] Mawet, D., Shelton, C., Wallace, J., Bottom, M., Kuhn, J., Mennesson, B., Burruss, R., Bartos, R., Pueyo, L., Carlotti, A., and Serabyn, E., "Demonstration of vortex coronagraph concepts for on-axis telescopes on the Palomar Stellar Double Coronagraph," in [*Space Telescopes and Instrumentation 2014: Optical, Infrared, and Millimeter Wave*], Oschmann, Jacobus M., J., Clampin, M., Fazio, G. G., and MacEwen, H. A., eds., *Society of Photo-Optical Instrumentation Engineers (SPIE) Conference Series* **9143**, 91432T (Aug. 2014).

[26] Bottom, M., Shelton, J. C., Wallace, J. K., Bartos, R., Kuhn, J., Mawet, D., Mennesson, B., Burruss, R., and Serabyn, E., "Stellar Double Coronagraph: A Multistage Coronagraphic Platform at Palomar Observatory," *PASP* **128**, 075003 (July 2016).

[27] Ruane, G., Mawet, D., Jewell, J., and Shaklan, S., "Performance and sensitivity of vortex coronagraphs on segmented space telescopes," in [*Society of Photo-Optical Instrumentation Engineers (SPIE) Conference Series*], *Society of Photo-Optical Instrumentation Engineers (SPIE) Conference Series* **10400**, 104000J (Sept. 2017).

[28] Jenkins, C., "Optical vortex coronagraphs on ground-based telescopes," *MNRAS* **384**, 515–524 (Feb. 2008).

[29] Ruane, G., Riggs, A., Coker, C. T., Shaklan, S. B., Sidick, E., Mawet, D., Jewell, J., Balasubramanian, K., and Stark, C. C., "Fast linearized coronagraph optimizer (FALCO) IV: coronagraph design survey for obstructed and segmented apertures," in [*Space Telescopes and Instrumentation 2018: Optical, Infrared, and Millimeter Wave*], Lystrup, M., MacEwen, H. A., Fazio, G. G., Batalha, N., Siegler, N., and Tong, E. C., eds., *Society of Photo-Optical Instrumentation Engineers (SPIE) Conference Series* **10698**, 106984U (Aug. 2018).